Self-layering of (Ti,Al)N by interface-directed spinodal decomposition of (Ti,Al)N/TiN multilayers: First-principles and experimental investigations

Chun Hu [a,b], Jie Zhang [a], Li Chen [a,c,*], Yu X. Xu [a], Yi Kong [a,*], Jian W. Du [a], Paul H. Mayrhofer [b]

[a] State Key Laboratory of Powder Metallurgy, Central South University, Changsha 410083, China
[b] Institute of Materials Science and Technology, TU Wien, Getreidemarkt 9, Vienna A-1060, Austria
[c] Zhuzhou Cemented Carbide Cutting Tools Co., LTD, Zhuzhou 412007, China

HIGHLIGHTS

- (Ti,Al)N/TiN multilayers show interface-directed spinodal decomposition.
- (Ti,Al)N sublayers within (Ti,Al)N/TiN reveal self-layering during annealing.
- *Ab initio* predicts the interface-directed spinodal decomposition.
- The layered arrangement provides a higher hardness of (Ti,Al)N/TiN multilayer.

GRAPHICAL ABSTRACT
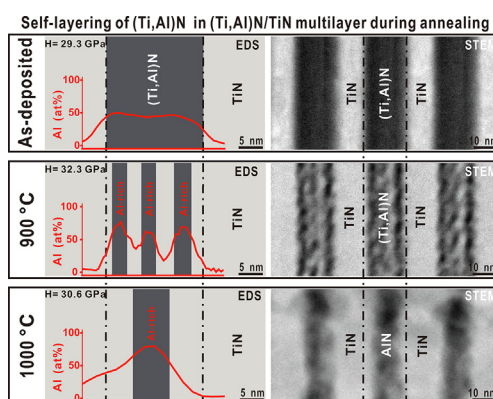
ABSTRACT

Supersaturated (Ti,Al)N materials with face centered cubic (fcc) structure offer unique combinations of thermal stability and mechanical properties. However, their thermally-induced decomposition processes are crucial for extracting their full potential. Detailed experimental studies by X-ray diffraction and transmission electron microscopy reveal that the formation of the thermodynamically stable wurtzite-type w-AlN starts with 1000 °C at 100 °C lower annealing temperatures (T_a) when applying a multilayer-concept with TiN to form (Ti,Al)N/TiN multilayers. Nevertheless, the hardness of (Ti,Al)N/TiN multilayers peaks with 32.3 ± 1.0 GPa at a 100 °C higher T_a (900 °C) than the (Ti,Al)N coating, and the hardness declining trend with increasing T_a is milder. This is because the (Ti,Al)N decomposes towards a layered structure of Al-rich and Ti-rich regions, when coherently grown with fcc-TiN. *Ab initio* calculations highlight that Al within the (Ti,Al)N layers preferentially diffuses away from the coherent interface with the TiN layers. Thus, out of one (Ti,Al)N layer more layers form, and even upon the phase-transformation of the Al-rich layers to w-AlN, their layered structure remains. Together, the computational and experimental results suggest that the layered arrangement provides a higher resistance against dislocation glide and is beneficial for the coating integrity.

* Corresponding authors at: State Key Laboratory of Powder Metallurgy, Central South University, Changsha 410083, China (L. Chen).
 E-mail addresses: chenli_927@126.com (L. Chen), yikong@csu.edu.cn (Y. Kong).

1. Introduction

(Ti,Al)N coatings are well-known materials applied to industrial cutting tools owing to the combination of high hardness, excellent corrosion resistance, and especially the age-hardening ability resulting from spinodal decomposition [1–4]. The thermal decomposition process of (Ti,Al)N, which involves spinodal decomposition into isostructural Ti-rich and Al-rich domains and the following formation of stable face-centered cubic (fcc-) TiN as well as wurtzite-type (w-) AlN, has been intensively studied by experiments and modeling [1–3,5]. (Ti,Al)N coatings with varied Al contents reveal broad composition and temperature ranges for spinodal decomposition [6–8]. The lattice mismatch and elastic difference among the isostructural Ti-rich, Al-rich domains, and remaining (Ti,Al)N matrix result in coherency strains, which enhance coating hardness by effectively impeding dislocation movement [9–12]. However, with elevating the annealing temperature or prolonging the annealing time, the cubic Al-rich domains transform to w-AlN with a concomitant volume expansion [13,14]. This transformation leads to the decline in hardness [15,16] due to the relatively lower hardness of w-AlN (14–20 GPa) [17] compared with fcc-(Ti,Al)N.

Multilayer architectures are promising to tailor the performance of hard coatings owing to the combination of dislocation interference at interfaces [18], strain effects [19], Hall-Petch strengthening [20], and epitaxial stabilization [21], which lead to superior hardness and thermal stability over the corresponding monolithic counterparts. Adding the multilayer concept to (Ti,Al)N-based coatings allows for a further optimization of their properties and enables them to be used for even more severe applications such as high-speed and dry cutting. Amongst the various (Ti,Al)N-based multilayers, (Ti,Al)N/TiN has attracted broad attention for its excellent mechanical properties [22] and machining performances [23]. Knutsson et al. studied the thermal decomposition products of arc evaporated (Ti,Al)N/TiN multilayers, claiming a spinodal-type decomposition of $Ti_{1-x}Al_xN$ sublayers into fcc Ti-rich and Al-rich domains [24]. They also reported thermally enhanced mechanical properties of $Ti_{0.34}Al_{0.66}N$/TiN multilayers, which were ascribed to particle confinement and coherency stresses from TiN sublayers [22]. In $Ti_{0.34}Al_{0.66}N$/TiN multilayers, spinodal decomposition starts at a lower temperature than for (Ti,Al)N, and the transformation from Al-rich fcc-structured domains to w-AlN is suppressed [22]. Especially, surface-directed spinodal decomposition at (Ti,Al)N/TiN interfaces was observed via atom probe tomography (APT) and scanning transmission electron microscopy (STEM) studies [25]. They observed the formation of AlN-rich and TiN-rich layers parallel to the $Ti_{0.34}Al_{0.66}N$–TiN interface, during the thermal decomposition route. An explanation of the above phenomenon owes to the so-called surface-directed spinodal decomposition (SDSD) that surfaces result in a wave vector directed of material with spinodal decomposition potential. The SDSD was observed in polymers [26,27], metals [28], and ceramics [29,30]. However, the role of interfaces during spinodal decomposition in multilayers is not systematically investigated, which would be important not only for the microstructure evolution but also the design of coatings. Therefore, interface-directed spinodal decomposition (IDSD) [31] rather than SDSD was considered here to elucidate the role of interfaces within multilayers and to distinguish their effect from general surfaces, like surfaces during growth of films [32].

The mechanisms behind IDSD in (Ti,Al)N/TiN multilayers still miss detailed data for their energetic and kinetic aspects. Besides those, also observations of the thermally-induced interface and microstructure evolution in (Ti,Al)N/TiN multilayers are missing.

Here we use a combination of theoretical and experimental methods for such studies. Transmission electron microscopy (TEM), scanning TEM (STEM), and high-resolution TEM (HRTEM) were utilized to observe the morphological changes of (Ti,Al)N/TiN multilayers and (Ti,Al)N coating upon thermal treatment in the range 800–1200 °C. *Ab initio* calculations provide explanations at the atomic scale that the diffusion of Al and Ti is strongly influenced by the interfaces. These studies are complemented by nanoindentation experiments for obtaining the hardness variation upon annealing. The combination of these studies allows to draw a complete picture of the interface-diffusion driven evolution within (Ti,Al)N/TiN multilayers – leading to a decreased (Ti,Al)N-to-TiN layer thickness ratio upon annealing – and its consequence on mechanical properties.

2. Computational and experimental details

2.1. Experimental methods

(Ti,Al)N/TiN multilayers and (Ti,Al)N coatings were prepared using an industrial cathodic arc evaporation system (Rapid Coating System, RCS, Balzers, Liechtenstein). The sketch map of the deposition system can be found in a previous work [33]. The ultrasonically pre-cleaned substrates (cemented carbides, low-alloy steel foils, tungsten plates) were mounted onto a two-fold rotatable substrate holder. After reaching a base pressure (in the main chamber) below 1.0×10^{-3} Pa, the chamber temperature was increased to 500 °C, and after reaching 500 °C, the substrates were Ar-ion etched for about 30 min at a pressure of ~ 0.3 Pa and by applying -180 V DC. The (Ti,Al)N/TiN multilayers and the (Ti,Al)N coatings were prepared in a flowing N_2 atmosphere (99.99 % purity, deposition pressure of ~ 3.2 Pa), and by applying a substrate bias potential of -40 V. The (Ti,Al)N layers of the (Ti,Al)N/TiN multilayer and the (Ti,Al)N coating were obtained by applying arc currents of 180 A to the $Ti_{0.50}Al_{0.50}$ cathodes. The TiN layers were obtained by applying arc currents of 160 A to the Ti cathodes. For the (Ti,Al)N/TiN multilayers, four of the six cathodes were equipped with $Ti_{0.50}Al_{0.50}$ and two with Ti (neighboring ones). The (Ti,Al)N coatings were obtained with the same setup but without operating the Ti cathodes.

A differential scanning calorimeter (DSC, Netzsch-STA 409C) was utilized to heat powdered coating samples (which were obtained by chemically dissolving the low-alloy steel foil on which they had been deposited) from room temperature (RT) to a given annealing temperature (T_a = 800, 900, 1000, 1100, 1200, 1300, and 1450 °C) in flowing Ar atmosphere (99.9 purity, flowing rate of 20 sccm) by 10 K/min. After reaching T_a, the samples were immediately cooled down by 50 K/min (down to 150 °C, after which the cooling rate decreased). The coatings onto W plates were heated in a CCD533R furnace from RT to T_a = 800, 900, 1000, 1100, and 1200 °C by 10 K/min with an isothermal segment at T_a of 30 min, after which the heater was turned off (resulting in a cooling rate of greater than 50 K/min down to 100 °C). The chemical compositions of as-deposited coatings were obtained by energy dispersive X-ray spectroscopy (EDS, Oxford Instruments X-Max), being attached to a scanning electron microscope (SEM, Zeiss Supra) and using an acceleration voltage of 25 kV. Qualitative characterization of the crystalline phases in the coatings in their as-deposited state and after annealing is obtained via X-ray diffraction (XRD) of powdered coating samples (using a D8 advance diffractometer, Cu Kα radiation, λ = 1.541 Å, operated at 40 kV and 40 mV, in Bragg − Brentano configuration).

The microstructure and chemical compositions of the as-deposited and annealed coatings (on W plates) were investigated

by TEM, HRTEM, and STEM using an FEI Titan G2 60–300 operated at 300 kV. The EDS linescan results of as-deposited and annealed TiAlN/TiN samples were actualized by STEM, which provide the Ti and Al concentrations on metal sublattice. Indentation hardness (H) values of these samples were derived from analyzing the load–displacement curves with a Poisson's ratio of 0.3 corresponding to TiN [34] – according to Oliver and Pharr [35] – obtained from nanoindentation (Anton Paar NHT^2) with a maximum load of 15 mN and a Berkovich diamond tip. Each data point is the mean value of more than 20 indentations per sample. More detailed information on obtaining the coating powder and preparing the TEM samples, as well as the deposition equipment is described in [36].

2.2. Calculation details

Diffusion mechanisms were investigated by density functional theory (DFT) calculations as implemented in the Vienna ab-initio simulation package (VASP) [37]. The electron–electron exchange and correlation interactions were studied by approximation of generalized gradient approximation (GGA) method parameterized by Perdew-Burke-Ernzerhof (PBE) version [38]. The valence electronic configurations used in the pseudopotentials were Ti $3d^24s^2$, Al $3s^23p^1$ and N $2s^22p^3$, respectively. The ion–electron interaction was described by the projected augmented wave (PAW) method [39,40], with a corresponding plane-wave cutoff energy of 500 eV. The Brillouin-zone was sampled via $10 \times 10 \times 10$ k-point mesh by Monkhorst-Pack method [41]. The convergence criteria of electronic self-consistency energy and the force between atoms for structure optimization were 10^{-5} eV and -0.05 eV/Å.

The vacancy diffusion mechanism of metal atoms adopted within this study has been proven as the main reason for spinodal decomposition of TiAlN-based coatings [5,42–44]. The calculation of atomic diffusion is based on the climbing image nudged elastic band (CI-NEB) theory, implemented by transition state tools for VASP (VTST). An atom diffuses from its initial equilibrium lattice position (referred to as initial state, IS) to the neighboring equilibrium position (referred to as the final state, FS) through a state corresponding to a saddle point (referred to as the transition state, TS) along the diffusion path [45,46]. Fig. 1 presents the geometric diagram of diffusion pathways for metal atoms in the Ti$_{0.5}$Al$_{0.5}$N/TiN multilayer. The pathways of Al and Ti into a nearest neighbor (NN) vacancy within the Ti$_{0.50}$Al$_{0.50}$N layer are pictured in Fig. 1a

and b, respectively. Those for Ti into NN vacancies in the TiN layer are shown in Fig. 1c and d. The corresponding sketch maps of diffusion processes in TiN and Ti$_{0.5}$Al$_{0.5}$N are depicted in the supplementary material (Fig. S1 and Fig. S2, respectively). To simplify notations, the diffusion of M1 atom at P1 site towards nearest neighbor M2 vacancy at P2 site on (XXX) plane is denoted as $M1_{P1} \rightarrow V_{M2}^{P2}(XXX)$. For example, $Ti_{C2} \rightarrow V_{Ti}^{D2}(100)$ in Fig. S1 represents the diffusion of Ti atom at C2 sites into nearest neighbor Ti vacancies at D2 sites on (100) plane.

3. Results and discussion

3.1. Chemical compositions

To simplify notations, all coatings are standardized to 50 at. % nitrogen as the metal/nitrogen atomic ratio is 1.00 ± 0.08. The nominal chemical composition of coatings obtained from four Ti$_{0.5}$Al$_{0.5}$ cathodes is Ti$_{0.52}$Al$_{0.48}$N. For easier reading, this Ti$_{0.52}$Al$_{0.48}$N coating is referred to as (Ti,Al)N throughout this work. Correspondingly, the Ti-Al-N layer within the (Ti,Al)N/TiN multilayers is also referred to as (Ti,Al)N.

3.2. Crystallography

The (Ti,Al)N coating is single-phase fcc structured in the as-deposited state (Fig. 2a), with the major diffraction peaks between the standard positions of fcc-TiN (ICDD 00-038-1420) and fcc-AlN (ICDD 00-046-1200). Annealing at T$_a$ = 800 °C triggers a slight shift of the XRD peaks to higher diffraction angles, suggesting for macro strain-reduction, which is typically an indication for recovery processes – if the overall XRD response otherwise does not change too much – where defects such as vacancies and dislocations arrange towards lower energy sites [15,47]. This is also supported by the slightly reduced width of the XRD peaks, which is generally associated with reduced microstrains and increased coherently diffracting domain sizes, two characteristics for recovery processes [48]. Increasing T$_a$ to 900 °C causes a shoulder-development on both sides of the (1 1 1) and (2 0 0) XRD peaks, which stems from the formation of mutual coherent Ti-rich and Al-rich domains via spinodal decomposition [1–3,49,50]. With T$_a$ = 1000 °C, the shoulders further increase in intensity and sharpen, suggesting ongoing spinodal decomposition. After annealing at 1100 °C, a minor diffraction signal at 2θ ∼ 33.2° suggests the formation of the stable wurtzite-type structure of AlN (w-AlN, ICDD 00-025-1133). Increasing T$_a$ to
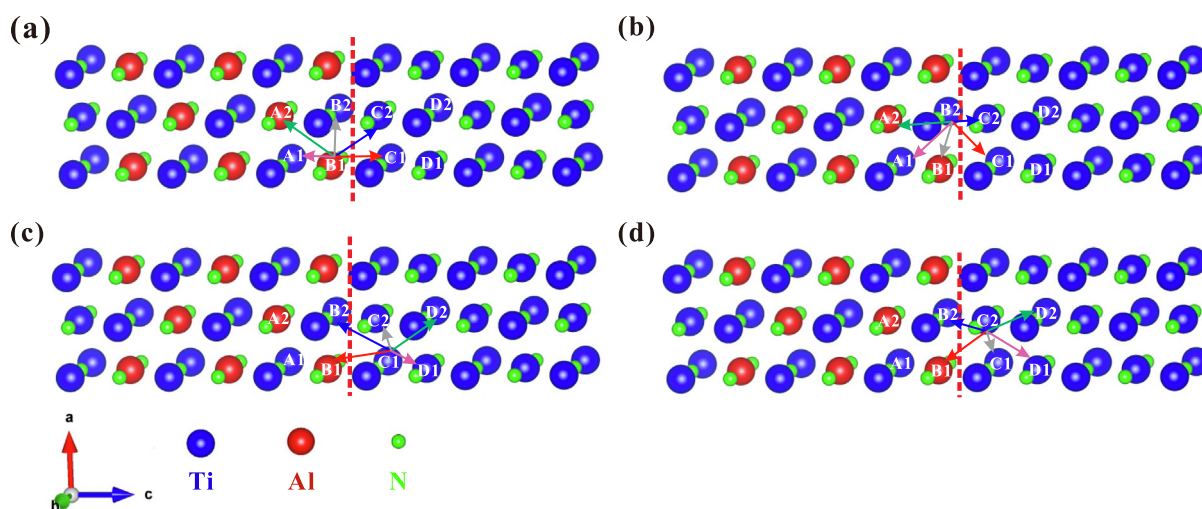

Fig. 1. Geometric diagram of diffusion pathways for (a) Al_B1, (b) Ti_B2, (c) Ti_C1, and (d) Ti_C2 metal atoms in the Ti$_{0.50}$Al$_{0.50}$N/TiN multilayer.
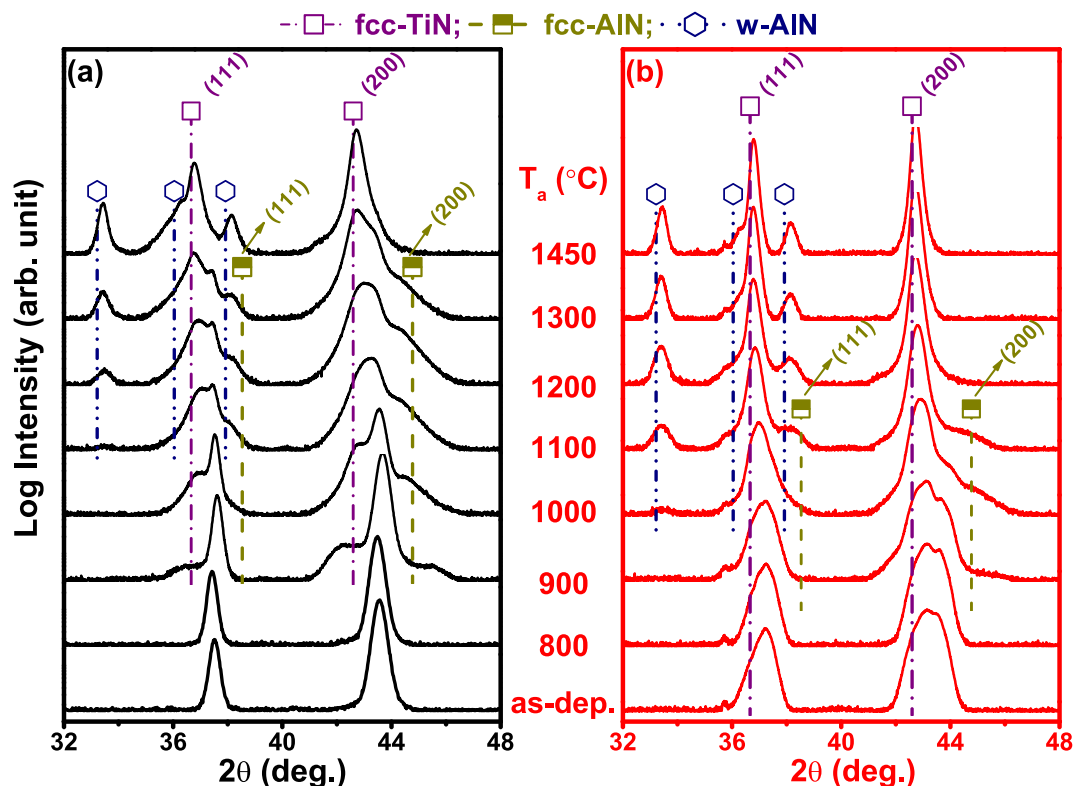
Fig. 2. XRD patterns of the (a) (Ti,Al)N coating and (b) (Ti,Al)N/TiN multilayer (in powdered form after removal from their low-alloy steel foils) after annealing to T_a (given at the individual patterns), without an isothermal holding segment.

1200 and 1300 °C leads to continuous increasing diffraction intensity of w-AlN. Simultaneously, the intensities of the XRD peaks indicative for fcc-AlN decrease while those indicative for fcc-TiN increase. Finally, after annealing at 1450 °C, no original solid solution fcc-(Ti,Al)N can be detected anymore, confirming a completed decomposition into their thermodynamically stable constituents w-AlN and fcc-TiN.

The XRD pattern of the as-deposited (Ti,Al)N/TiN multilayer shows cumulative features of the fcc-(Ti,Al)N and fcc-TiN layers for the (111) and (200) planes, which are captured in the diffraction range presented in Fig. 2b. Annealing at 800 °C causes a more separated response by the individual layers to the XRD investigation, see the slightly separated peaks at the (200) orientation. The small XRD peaks at the positions of fcc-TiN and fcc-AlN for the 900 °C annealed samples suggest – in agreement with the (Ti,Al)N coating – that spinodal decomposition of the (Ti,Al)N sublayers into Ti-rich and Al-rich domains started. When it comes to the decomposition process of supersaturated fcc-structured (Ti,Al)N towards fcc-TiN and fcc-AlN, the concomitant changes in stresses/strains need to be considered. Generally, fcc-(Ti,Al)N exhibits a positive deviation from Vegard's rule, which is a linear interpolation between the lattice constants of fcc-TiN and fcc-AlN [43,51]. The lattice constant – obtained from the corresponding XRD peak positions – for fcc-Ti$_{0.52}$Al$_{0.48}$N is 4.160 Å, and thus reveals a positive deviation from Vegard's rule, which would suggest 4.147 Å for fcc-Ti$_{0.52}$Al$_{0.48}$N, using 4.242 Å for fcc-TiN (ICDD 00–038-1420) and 4.045 Å for fcc-AlN (ICDD 00–046-1200). Consequently, the spinodal decomposition from fcc-(Ti,Al)N into coherent fcc-TiN and fcc-AlN is connected with a reduction in overall specific volume (volume per atom), leading to increased tensile strains [43]. Thus, residual tensile strains within the (Ti,Al)N layers would even suppress spinodal decomposition whereas compressive residual stresses would promote this. Notable is that the resid-

ual stresses (tensile/compressive) can be different in the directions parallel and perpendicular to the interface between TiN and AlN [52]. Coherence strains between fcc-TiN and fcc-(Ti,Al)N layers would leave the latter under tensile strains, because fcc-(Ti,Al)N has a smaller lattice parameter than fcc-TiN. This simplified picture suggests that the spinodal decomposition of the (Ti,Al)N layers of the multilayer should be retarded. However, as spinodal decomposition requires the diffusion of Al and Ti, any process promoting their diffusion also promotes spinodal decomposition. This is in-line with phase-field simulations and differential scanning calorimetry studies of (Ti,Al)N/TiN multilayers [25], reporting about the promoting effect of interfaces on the spinodal decomposition of their (Ti,Al)N layers.

Contrary to the onset for spinodal decomposition, the formation of w-AlN can be detected for the (Ti,Al)N/TiN multilayer at an ~ 100 °C lower annealing temperature than for (Ti,Al)N, see the XRD pattern recorded after annealing at T_a = 1000 °C, Fig. 2b. This finding is different to the study of A. Knutsson et al. reporting about a suppressed formation of w-AlN for a Ti$_{0.34}$Al$_{0.66}$N/TiN multilayer with respect to the monolithically grown Ti$_{0.34}$Al$_{0.66}$N [22]. Contrary to their multilayers, in which the TiN layers are twice as thick as the (Ti,Al)N layers, in our multilayers the (Ti,Al)N layers are thicker, but also the Al-content of their (Ti,Al)N layers is higher and the overall bilayer period (18 nm) is lower. As reported in [53], the Al content of (Ti,Al)N influences the formation temperature of w-AlN. However, compared with the (Ti,Al)N sample, the (Ti,Al)N/TiN multilayer shows even two right-hand shoulders of the major (200) XRD peak. The explanation of which is addressed in the next chapter (concentrating on transmission electron microscopy). After annealing at 1100 °C, almost no fcc-AlN and fcc-(Ti,Al)N can be detected anymore and the diffraction intensities from w-AlN and fcc-TiN substantially increased. The XRD patterns recorded after annealing at 1200, 1300, and 1450 °C are essentially composed of

solely w-AlN and fcc-TiN phases, indicating a completed decomposition process. Thus, the XRD studies suggest that while the spinodal decomposition is initiated at a similar temperature for (Ti,Al)N and the (Ti,Al)N/TiN multilayer, the latter experiences an earlier formation of w-AlN. Additionally, also the decomposition into the stable constituents fcc-TiN and w-AlN is completed earlier for the (Ti,Al)N/TiN multilayer.

3.3. TEM investigations

3.3.1. (Ti,Al)N coatings

Cross-sectional bright-field (BF) transmission electron microscopy of the (Ti,Al)N coating annealed at $T_a = 800$ °C, Fig. 3a, clearly shows the pronounced columnar growth morphology with a column width of ∼ 200–500 nm. The SAED pattern, Fig. 3b, highlights the single-phase fcc structure. The corresponding STEM-HAADF image, Fig. 3c, and especially the higher magnification, Fig. 3d, show periodic nm-sized contrast differences, indicative for spinodal decomposition towards Al-rich and Ti-rich coherent domains [5,54,55]. After annealing at 900 °C, the columnar structure is still present, see the BF TEM image (Fig. 3e). However, the corresponding SAED investigation conducted with the same aperture size as for the 800 °C annealed sample (Fig. 3f) already indicates a reduced overall size of fcc grains. The mass contrast is especially pronounced along the grain boundaries, see the STEM-HAADF image Fig. 3g. The lamellar contrast along the growth direction stems from the 2-fold substrate rotation during the deposition process and the annealing-induced intensification of the defect contrast. The enrichment of Al at grain and column boundaries is consistent with three-dimensional atom probe tomography results of mag-

netron sputtered Ti-Al-N [2]. The higher magnification STEM-HAADF image (Fig. 3h) shows an increased contrast modulation as compared to the 800 °C annealed case (Fig. 3d), manifesting the ongoing spinodal decomposition. Even after annealing at 1000 °C, the columnar structure is still present (Fig. 3i) and also the SAED investigation (Fig. 3j) conveys fcc structure. However, the STEM-HAADF image (Fig. 3k) now clearly shows that especially the column boundaries are decorated with larger spherical precipitates (of lower mass). The size of these Al-rich domains varies between 4 and 20 nm, Fig. 3l.

Annealing at 1100 °C causes the Al-rich domains at the grain boundaries to coarsen to ∼ 11–45 nm, see Fig. 4a. HRTEM studies of such a region at the column boundary, Fig. 4b, prove their w-AlN nature by the lattice fringes and the semi-coherent growth with the fcc-Ti(Al)N remainder. The SAED pattern from this area, Fig. 4c, confirms the w-AlN structure. STEM-mapping profiles of this column boundary region, Fig. 4d, highlight the Al-enrichment (Fig. 4e) and Ti-depletion (Fig. 4f) along the column boundary. The N content only slightly correlates with the columnar structure, Fig. 4g. The slightly lower intensity of N along the column boundaries may also stem from the generally larger specific volume of w-AlN.

3.3.2. (Ti,Al)N/TiN multilayers

The as-deposited (Ti,Al)N/TiN multilayer exhibits a pronounced columnar grain morphology with clearly distinguishable alternating (Ti,Al)N and TiN layers, Fig. 5a. The STEM-HAADF investigation coincides well with the compositional fluctuations of the STEM-EDS line-scan, revealing a bilayer period of ∼ 32.8 nm consisting of ∼ 12.7-nm-thin TiN and ∼ 20.1-nm-thin (Ti,Al)N layers. The
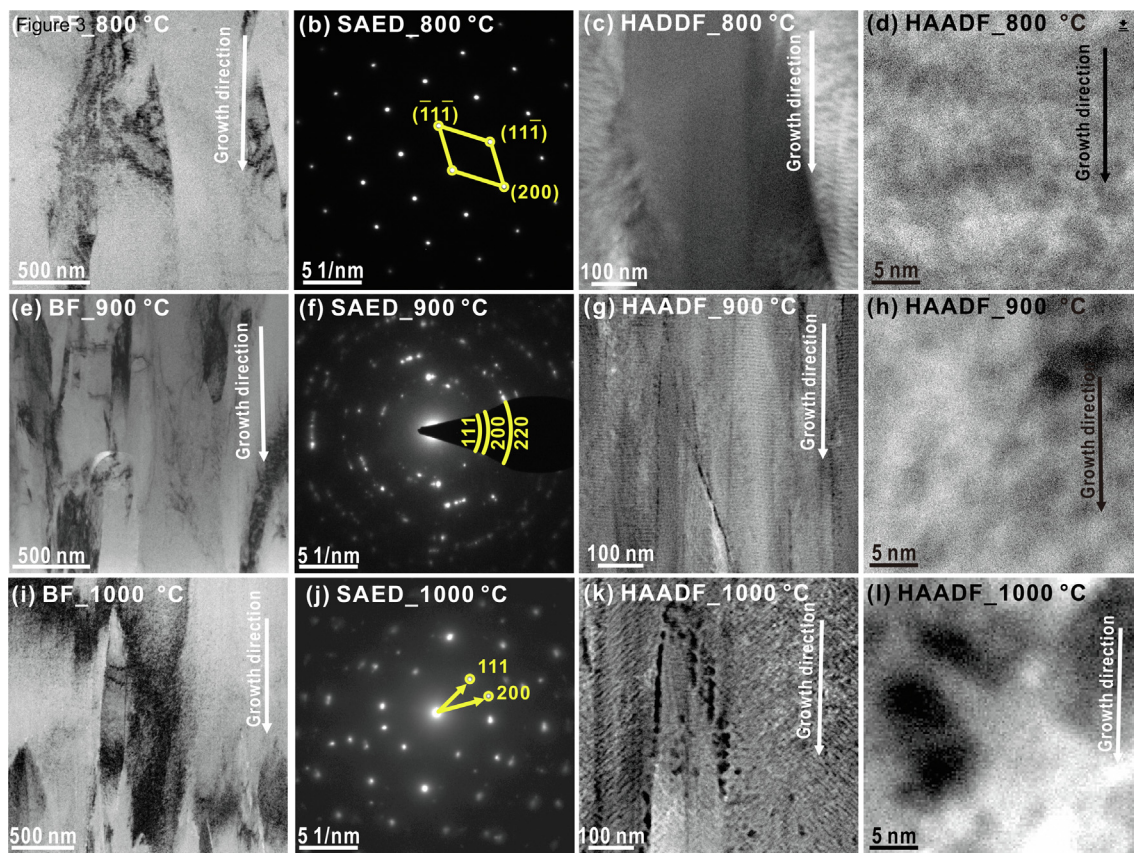

Fig. 3. Cross-sectional TEM investigations of the (Ti,Al)N coating annealed at 800, 900, and 1000 °C for 30 min: (a) BF image, (b) SAED pattern, (c) and (d) STEM-HAADF images of (Ti,Al)N annealed at 800 °C; (e) BF image, (f) SAED pattern, (g) and (h) STEM-HAADF images of (Ti,Al)N annealed at 900 °C; (i) BF image, (j) SAED pattern, (k) and (l) STEM-HAADF images of (Ti,Al)N annealed at 1000 °C.
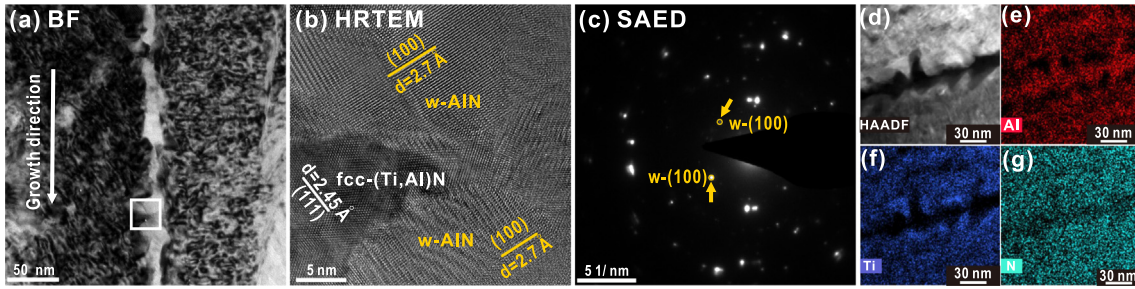
Fig. 4. Cross-sectional TEM investigations of the (Ti,Al)N coating annealed at 1100 °C for 30 min: (a) BF image, (b) HRTEM image of the area marked in (a), (c) SAED pattern of the center region in (a), (d) STEM-HAADF image with STEM-EDX mapping profiles of (e) Al, (f) Ti, and (g) N.
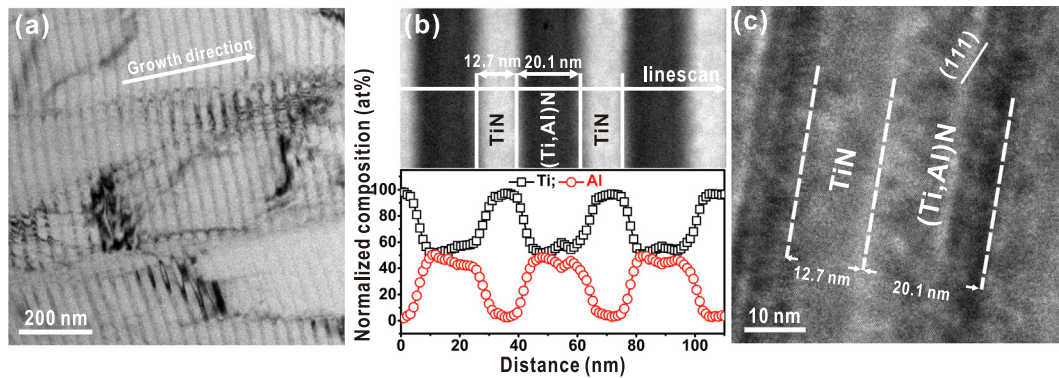

Fig. 5. Cross-sectional TEM investigations of the as-deposited (Ti,Al)N/TiN multilayer: (a) BF image, (b) STEM-HAADF image with STEM-EDX line-scan profile, and (c) HRTEM image.
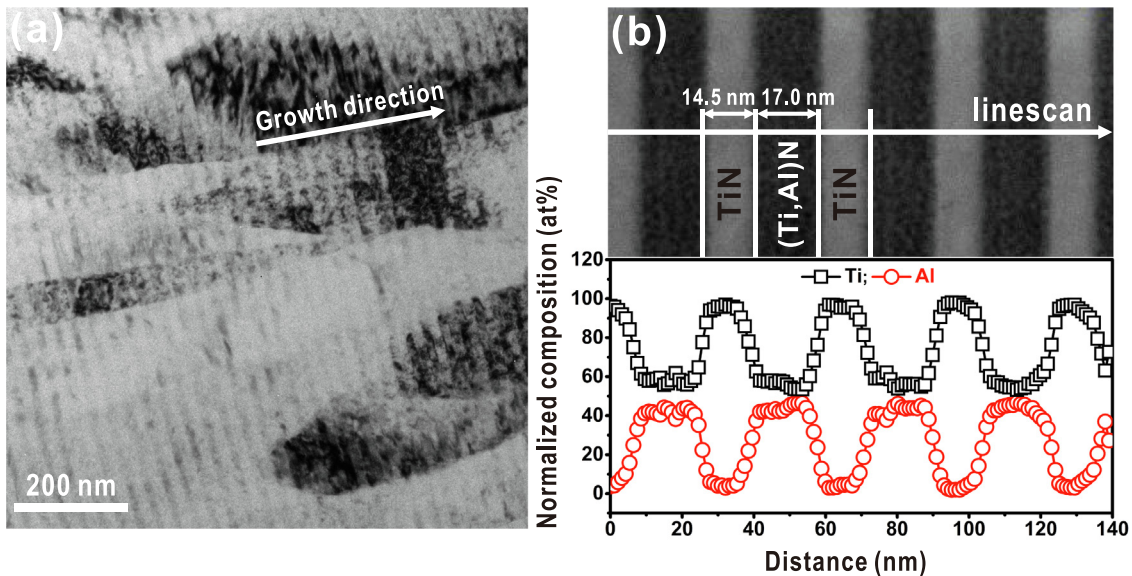

Fig. 6. Cross-sectional TEM investigations of the (Ti,Al)N/TiN multilayer after annealing at 800 °C for 30 min: (a) BF image and (b) STEM-HAADF image with STEM-EDX line-scan profile.

(Ti,Al)N/TiN layer thickness ratio is thus ∼ 1.6 in the as-deposited state. There are no detectable fluctuations of the metal elements within the individual (Ti,Al)N and TiN layers along the growth direction. HRTEM (Fig. 5c) demonstrates that the lattice fringes continuously expand across several adjacent layers, indicating epitaxial growth of the (Ti,Al)N and TiN layers.

Upon annealing to 800 °C, the interfaces between the (Ti,Al)N layers (dark contrast in Fig. 6a) and TiN layers (bright contrast in

Fig. 6a) are still smooth and parallel to each other. The BF TEM also shows large columnar grains with ∼ 100 nm width. The STEM investigation, Fig. 6b, clearly shows well-separated TiN and (Ti, Al)N layers of ∼ 14.5 and 17.0 nm thickness, respectively. Thus, the (Ti,Al)N/TiN layer thickness ratio noticeably decreases from the as-deposited value of ∼ 1.6 to ∼ 1.2 upon annealing at 800 °C. The STEM-EDS line scan verifies the decreased (Ti,Al)N layer thickness and increased TiN layer thickness, as compared to

the as-deposited state. Additionally, the elemental profile shows a smoother transition from the (Ti,Al)N to the TiN layers.

Upon increasing T_a to 900 °C, the thickness of the TiN layers further increases and that of the (Ti,Al)N layers decreases, while still keeping the overall columnar structure and parallel layer arrangement, Fig. 5a. STEM-HAADF investigations reveal comparable layer thicknesses of 16.6 nm for both layers, Fig. 5b. But now the Al fluctuation within the (Ti,Al)N layer is apparent with three consecutive peaks across their thickness, see the STEM-EDS line scan in Fig. 5b. This coincides with the general impression obtained from the STEM-HAADF image that next to the TiN layer there is an Al-rich layered region within the (Ti,Al)N layer. After which a Ti-rich layered region within the (Ti,Al)N layer is formed to be followed by an Al-rich layered region. This process resembles a spinodal decomposition as there is a diffusion against the concentration gradient (uphill-diffusion). But contrary to the spinodal decomposition within more homogenous (Ti,Al)N coatings – where the formation of Al-rich and Ti-rich domains is more statistically distributed (neglecting preferential sites at grain and column boundaries) – the coherent growth of (Ti,Al)N layers on TiN layers provides a changed boundary condition. In order to minimize the overall coherency strains – which would increase upon the formation of additional Al-rich and Ti-rich regions within the (Ti,Al)N layers – the spinodal decomposition of (Ti,Al)N regions next to the TiN layers will proceed by thickening the already present coherent TiN layers. This in further consequence naturally leads to the spinodal formation of Al-rich layers adjacent to that. This essentially resembles the already mentioned interface-directed spinodal decomposition, IDSD, which can also be understood by the strains present at the coherent interfaces between fcc-structured (Ti,Al)N and TiN. The lattice parameter a of fcc-Ti$_{1-x}$Al$_x$N continuously decreases from 4.24 Å (for fcc-TiN [ICDD 00–038-1420]) to 4.05 Å (for fcc-AlN [ICDD 00–046-1200]) with increasing Al-content $\times$ [56]. Thus, the formation of Ti-rich fcc-Ti$_{1-x+\Delta}$Al$_{x-\Delta}$N upon a spinodal decomposition of fcc-Ti$_{1-x}$Al$_x$N is promoted at tensile-strained regions – in the direct proximity to the TiN layers for our (Ti,Al)N/TiN multilayers. This phenomenon is also verified by *ab initio* calculations, presented in the following chapter.

The samples annealed at 1000 °C exhibit a more pronounced layered structure as those annealed at lower T_a, and the overall layer-thickness-ratio massively changes, comparing Fig. 8a with Fig. 7a. STEM-HAADF investigations capture the alternating formation of Ti-rich (bright contrast) and Al-rich (dark contrast) layers, Fig. 8b. The corresponding STEM-EDS line scan highlights a double-peak in the Al-profile, as already anticipated from the BF TEM (Fig. 8a) as well as STEM-HAADF (Fig. 8b) images. HRTEM investigations, Fig. 8c, confirm the wurtzite structure for the Al-rich layers and indicate even stacking faults within the fcc-structured Ti-rich layers (marked by arrows). Inverse Fast Fourier Transformation (IFFT) of an interface region between w-AlN and fcc-TiN layers (marked in Fig. 8d), indicates a semi-coherent growth of these phases with an orientation-relationship according to the studies by Rafaja et al. [57]. The STEM-EDS line scan suggests for about 8 Ti-rich layers over the distance of 280 nm, thus one stack of Ti-rich and Al-rich layers is about 35 nm wide. This nicely agrees with the following simplified assumption: The as-deposited bilayer period is 33 nm, which comprises 20-nm-thin fcc-Ti$_{0.52}$Al$_{0.48}$N and 13-nm-thin fcc-TiN. A simplified layered spinodal decomposition of the fcc-Ti$_{0.52}$Al$_{0.48}$N would result in 10-nm-thin fcc-AlN and 10-nm-thin fcc-TiN, from which 5 nm dock onto the existing fcc-TiN layer underneath and 5 nm onto the fcc-TiN layer above (seen from a fcc-Ti$_{0.52}$Al$_{0.48}$N layer sandwiched between two fcc-TiN layers). This essentially leaves us with a stack of 23-nm-thin fcc-TiN and 10-nm-thin fcc-AlN. If now the latter phase transforms to its thermodynamically stable wurtzite morphology (with the connected volume expansion by 28 %), the layer thickness increases to 12.8 nm. Hence, overall we would have 23.0 + 12.8 = 35.8 nm, in excellent agreement with the STEM-EDS line profile.

Annealing at 1100 °C causes the layered arrangement to slightly transform towards a more spherical formation of especially the minority component w-AlN, Fig. 9a. STEM-HAADF and the corresponding STEM-EDS maps, Fig. 9b, c, and d, respectively, prove that the more spherical regions are essentially AlN, being encapsulated in TiN. The HRTEM investigation, Fig. 9e, clearly indicates the fcc-structure for TiN and the wurtzite structure for AlN and the loss of the layered arrangement. The latter is based on the competing energies. Strain-energy minimization would favor the platelet or lamellar arrangement whereas surface-energy minimization
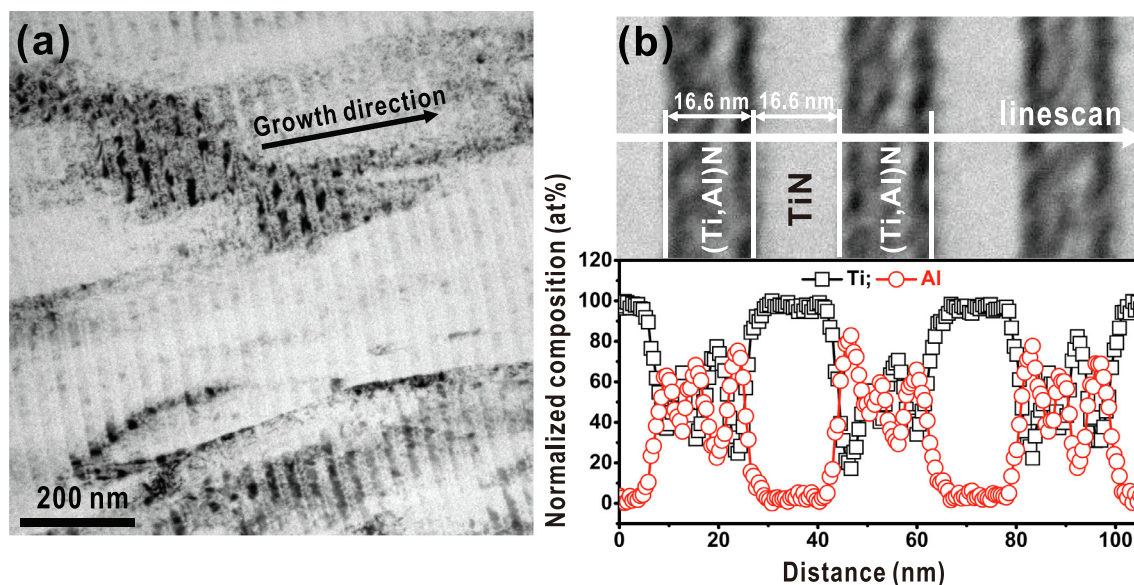

Fig. 7. Cross-sectional TEM investigations of the (Ti,Al)N/TiN multilayer after annealing at 900 °C for 30 min: (a) BF image and (b) STEM-HAADF image with STEM-EDX line-scan profile.
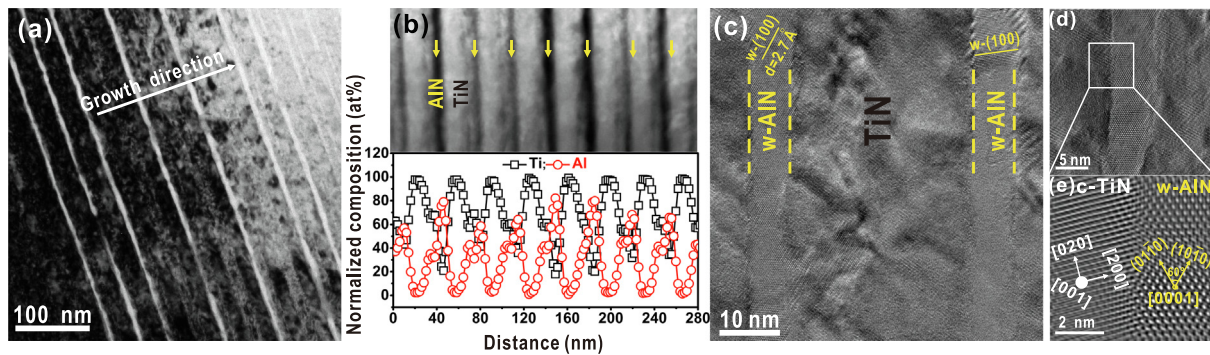
Fig. 8. Cross-sectional TEM investigations of the (Ti,Al)N/TiN multilayer after annealing at 1000 °C for 30 min: (a) BF image, (b) STEM-HAADF image with STEM-EDX line-scan profile, (c) and (d) HRTEM, and (e) IFFT images.
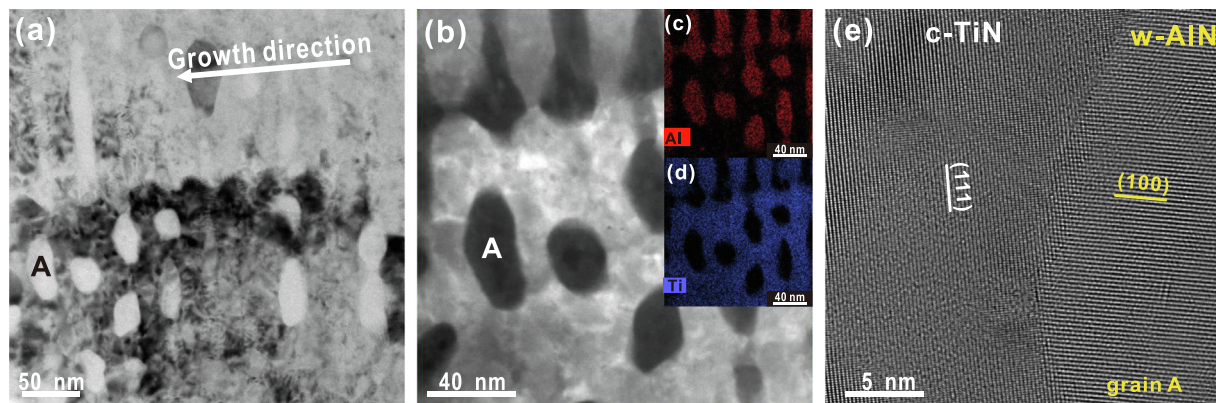

Fig. 9. Cross-sectional TEM investigations of the (Ti,Al)N/TiN multilayer after annealing at 1100 °C for 30 min: (a) BF image, (b) STEM-HAADF image STEM-EDX mapping profiles of (c) Al and (d) Ti, and (e) HRTEM image.

would favor the spherical formation of w-AlN. Especially at higher temperatures, the latter is possible due to the increased formation of misfit dislocations.

3.4. Ab-initio calculations

The detailed TEM studies clearly show that the spinodal decomposition of the (Ti,Al)N layers is influenced by the coherent interface with the TiN layers. To further elucidate the underlying mechanism of such an interface-directed spinodal decomposition process, *ab initio* calculations combining the climbing image-nudged elastic band (CI-NEB) method were used to investigate the atomic diffusion near the (Ti,Al)N/TiN interface.

Fig. S3 of the supplementary material illustrates the diffusion barriers of Ti along different diffusion pathways in a TiN supercell calculated by CI-NEB. The Ti → V_{Ti} (001) diffusion path reveals the highest barrier since only 4 atoms are truncated on the (001) plane while 20 atoms in each of the other two directions are truncated. The midpoint of the reaction coordinate corresponds to the highest value of the energy barrier, which is considered as the diffusion activation energy along specific diffusion paths [58]. Accordingly, the self-diffusion activation energy of Ti in TiN is 3.31 eV without considering the diffusion on the (001) plane. Fig. S4 of the supplementary material shows the diffusion energy barriers of Ti (Fig. S4a) and Al (Fig. S4b) in a $Ti_{0.50}Al_{0.50}N$ supercell along different diffusion paths. While the results from final state (FS) energy of the Ti → V_{Al} diffusion paths is positive, that of the Al → V_{Ti} diffusion paths is negative, indicating an energetically preferred diffusion of Al. Additionally, the diffusion process of Al → V_{Ti} (100) reveals the lowest activation energy of all diffusion processes considered. It is worth noting that under spring force, the Al atom leaves the

equilibrium position at first, which causes breaking of the Al-N bond and leaves an Al vacancy. Subsequently, as Al continues to diffuse into the adjacent Ti vacancies (V_{Ti}), the Al atom bonds with the surrounding N, leaving Al on the original Ti vacancy sublattice (Al_{Ti}). Thus, the corresponding diffusion of Al → V_{Ti} can also be denoted as $Al_{Al} + V_{Ti} \rightarrow V_{Al} + Al_{Ti}$.

Consequently, the spinodal decomposition process of (Ti,Al)N is triggered by the diffusion of Al. As diffusion at surfaces and interfaces is faster than in the lattice, the formation of Al-rich regions is typically detected first at column and grain boundaries [2,47,59], see also Fig. 4.

The diffusion barriers for atoms along different routes near the interface in (Ti,Al)N/TiN multilayer (Fig. 10) reveal the preferential diffusion of Al away from the interface towards the middle of the (Ti,Al)N layer. Ti atoms within the TiN layer (at the coherent interface with the (Ti,Al)N layer) preferably diffuse even across the interface. The diffusion barriers for Al at B1 to the internal positions A1 and A2 are relatively low (Fig. 10a), indicating that Al tends to diffuse to the internal region of (Ti,Al)N, away from the interface. The diffusion activation energy of Al → V_{Ti} (100) is lower than that of Al → V_{Al} (010), suggesting that it is easier for Al to diffuse to the Ti vacancy in (Ti,Al)N than to the Al vacancy. The activation energies for Ti at B2 to the interior positions A1 and A2 (Fig. 10b) also indicate an inward diffusion tendency of Ti away from the interface. But the diffusion activation energy of Ti → V_{Ti} (100) is lower than that of Ti → V_{Al} (010), so that Ti tends to diffuse to the Ti vacancy in (Ti,Al)N. If we now combine these results, with the addition that Al is faster, Al diffuses away from the interface to Ti vacancies closer to the middle of (Ti,Al)N. This leaves additional vacancies closer to the interface which are preferably occupied by Ti. Within the TiN layers (Fig. 10c and d), Ti tends to
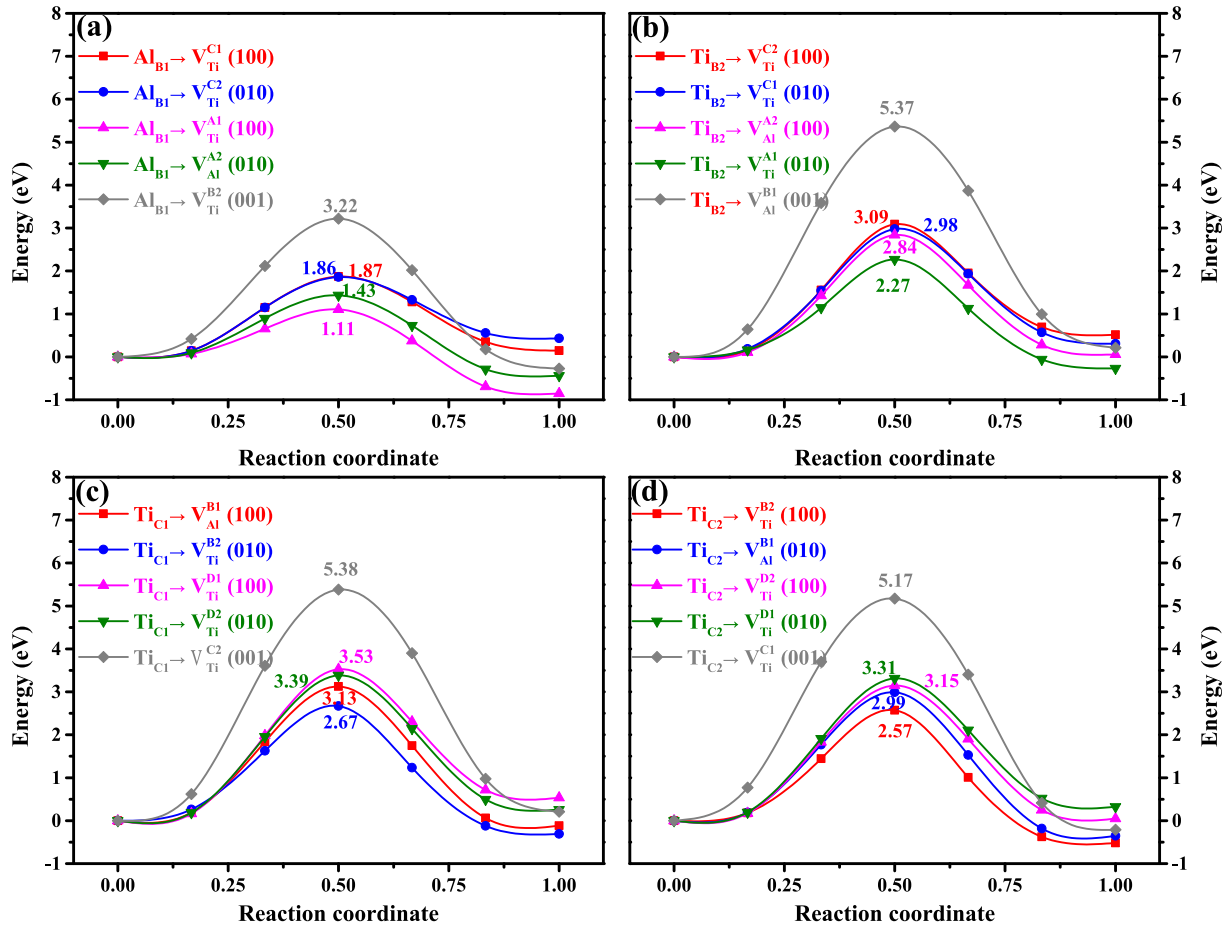
Fig. 10. Diffusion barriers as a function of the coordinate for different diffusion pathways of (a) Al_B1, (b) Ti_B2, (c) Ti_C1, and (d) Ti_C2 in the $Ti_{0.50}Al_{0.50}N/TiN$ supercell.

diffuse to the (Ti,Al)N layer across the interface, as the activation energies of Ti at C1 (or $C2$) to the B1 and B2 positions in (Ti,Al)N are relatively low. The route Ti → V_{Ti} (0 1 0) reveals the lowest diffusion barrier, manifesting that Ti intends to diffuse to Ti vacancies instead of Al vacancies of the (Ti,Al)N layer. The preferential inward diffusion of Al within (Ti,Al)N and the diffusion of Ti towards the interface in TiN – induced by the (Ti,Al)N–TiN interface – coincides well with TEM investigations. Upon annealing at 800 °C (Fig. 6b), Ti-rich layers form at the initial interface to the TiN layer, so that the thickness of the TiN layer increases at the expense of the (Ti,Al)N layer. Furthermore, with the intensified diffusion of Al and Ti at 900 °C, two Al-rich layers form in (Ti,Al)N and the thickness of the TiN layer further increases (Fig. 7b). Consequently, Al vacancies exist near the initial (Ti,Al)N–TiN interface, which induces the diffusion of Ti within (Ti,Al)N to the interface and sustains the thickening of the TiN layer.

The detailed average activation energy and driving force, the energy difference between the final state and the initial state, of the different diffusion routes in TiN, $Ti_{0.5}Al_{0.5}N$, and $Ti_{0.5}Al_{0.5}N/TiN$ also confirm the interface induced spinodal decomposition in multilayer structure. To avoid making the paper lengthy, the related discussions are given in supplementary materials (Table S1 and S2). In short, the introduction of TiN layer obviously promotes the inward diffusion of Al and Ti in (Ti,Al)N sublayers.

3.5. Hardness

The detailed TEM investigations – supported by *ab initio* calculations – help to understand the annealing-induced hardness evolution of the (Ti,Al)N/TiN multilayer with respect to the (Ti,Al)N
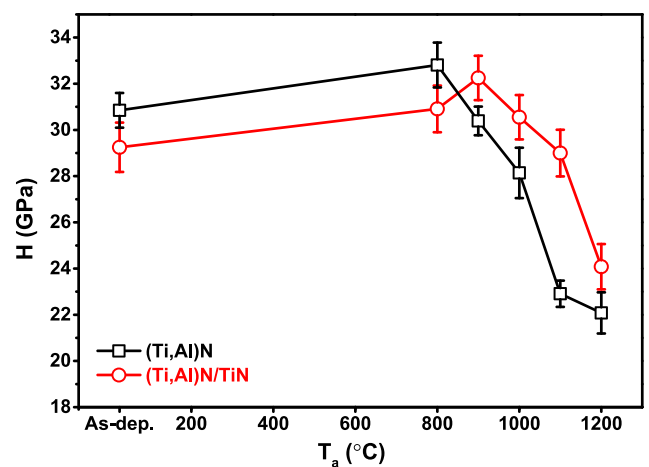
coating, Fig. 11. In agreement with previous reports, the (Ti,Al)N coating experiences a hardness increase upon annealing due to the well-studied spinodal decomposition to form coherent Ti-rich and Al-rich domains [1–3]. The lattice parameter and elastic constants variation with the Al-content [56] lead to coherency strains [43], which together with the formed domains effectively retard dislocation mobility and thereby harden the material [1]. For the (Ti,Al)N coating investigated here, this causes the hardness to

Fig. 11. Indentation hardness of the (Ti,Al)N coating and the (Ti,Al)N/TiN multilayer after annealing at T_a for 30 min (coatings on W plates).

increase from 30.9 ± 0.8 GPa to 32.8 ± 1.0 GPa when annealed at 800 °C (for 30 min). This same sample is investigated by TEM and shows all signs of spinodal decomposition, yet without any signs for w-AlN. With further increasing T_a to 900 and 1000 °C, the hardness declines to 30.4 ± 0.6 and 28.1 ± 1.1 GPa, respectively, which is also commonly observed due to further coarsening of the domains and the reduced interference with dislocations. Further increasing the annealing temperature to 1100 °C causes the precipitation of w-AlN (Fig. 4), initiating a drop in hardness to 22.9 ± 0.6 GPa. The wurtzite-type structure of AlN (w-AlN) is much softer than the metastable fcc-AlN modification. After annealing at 1200 °C (for 30 min), the hardness is 22.1 ± 0.9 GPa, thus still higher than for bulk ceramic TiN (~17 GPa [60]).

In the as-deposited condition, the hardness of the (Ti,Al)N/TiN multilayer is 29.3 ± 1.1 GPa, and thus according to the rule of mixture. As presented, their (Ti,Al)N-to-TiN layer thickness ratio is 1.6, and using this relation the estimated hardness would be 29.9 GPa (with 28.4 ± 0.6 GPa for TiN [33]). Although in general the H–vs–T_a curve of the (Ti,Al)N/TiN multilayer is similar to that of (Ti,Al)N, there are distinct and important differences. The hardness peaks (32.3 ± 1.0 GPa) with T_a = 900 °C, thus at a 100 °C higher temperature, although TEM studies indicate that the spinodal decomposition process is also initiated at already 800 °C. Even more important is that the hardness decline after the peak-value is less pronounced and still allows for 29.0 ± 1.0 GPa with T_a = 1100 °C, although the formation of w-AlN can already be detected with T_a = 1000 °C (Fig. 8). The distinct difference to (Ti,Al)N is, that for the (Ti,Al)N/TiN multilayer the Al-rich regions as well as w-AlN (when annealed at higher temperatures) are layered. Such layered structures would allow for more effective dislocation interference than spherical-like precipitates, especially for loading parallel to the layers (like the indentation of our coatings). A well-known and well-studied example would be Pearlite and spheroidized Pearlite (the latter being much softer, in German this is even called "weichgeglühter Perlit", thus softened Pearlite). Similarly, Knutsson et al. [22] also reported a wider temperature with high hardness in $Ti_{0.34}Al_{0.66}N$/TiN multilayers due to the suppressed spherical precipitation and growth of AlN precipitates. Annealing the (Ti,Al)N/TiN multilayer at 1100 °C initiates the spheroidization of the w-AlN layers (to minimize the overall surface and interface energy contribution) and the hardness decreases to 29.0 ± 1.0 GPa. Ongoing spheroidization during annealing at 1200 °C further reduces the hardness to 24.1 ± 1.0 GPa.

4. Conclusions

The spinodal decomposition behaviors of a (Ti,Al)N coating and a (Ti,Al)N/TiN multilayer were comparatively studied by XRD, TEM, nanoindentation, and *ab initio* calculations. Contrary to the (Ti,Al)N coating, which is classified by a randomly distributed formation of Al-rich and Ti-rich domains via spinodal decomposition but a bit more triggered at the column and grain boundaries due to the increased diffusivity here, the (Ti,Al)N/TiN multilayer exhibits a layered arrangement of these Al-rich and Ti-rich domains. The experimental results obtained are nicely supported by *ab initio* calculations combining the CI-NEB method, which suggest a preferential diffusion of Al from the coherent (Ti,Al)N–TiN interface towards the middle of (Ti,Al)N.

XRD and TEM results reveal that the temperature at which w-AlN forms, is 100 °C lower for the (Ti,Al)N/TiN multilayer than for the (Ti,Al)N coating. For the latter, w-AlN preferentially forms at grain and column boundaries, while for the (Ti,Al)N/TiN multilayer, w-AlN forms with a unique layered structure parallel to the original coherent interfaces between fcc-(Ti,Al)N and fcc-TiN. This self-layering mechanism is driven by the interface-directed

spinodal decomposition between the fcc (Ti,Al)N and TiN layers. The formation of this layered structure can be explained by *ab initio* combing the CI-NEB method, which predicts the preferential diffusion of Al from the coherent interface towards the middle of (Ti,Al)N. Thus, Ti-rich layers are formed along the initial (Ti,Al)N–TiN interface and thereby the layer-thickness-ratio between (Ti,Al)N and TiN decreases from 1.6 (as-deposited) to 1.2 (800 °C).

At 900 °C, more layers are observed through the intensified diffusion process. Two Al-rich layers form inside the (Ti,Al)N layer due to the preferential inward diffusion of Al from both sides of the coherent interfaces with fcc-TiN. Although Ti also tends to diffuse away from the interface towards the middle of (Ti,Al)N, Al is faster (as suggested by calculations) and leaves vacancies behind, into which preferentially Ti diffuses. Hence, the thickness of the TiN layers increases and within the (Ti,Al)N layers additional Al-rich and Ti-rich layers form. Even upon the formation of w-AlN at 1000 °C, this unique layered structure still remains within the (Ti,Al)N/TiN multilayer. This layered structure is more resistant against mechanical loading than the more random and spherical formation of w-AlN within the (Ti,Al)N coating.

Data availability

The data that support the findings of this study are available from the corresponding author upon reasonable request.

Declaration of Competing Interest

The authors declare that they have no known competing financial interests or personal relationships that could have appeared to influence the work reported in this paper.

Appendix A. Supplementary material

Supplementary data to this article can be found online at https://doi.org/10.1016/j.matdes.2022.111392.

References

[1] P.H. Mayrhofer, A. Hörling, L. Karlsson, J. Sjölén, T. Larsson, C. Mitterer, L. Hultman, Self-organized nanostructures in the Ti–Al–N system, Appl. Phys. Lett. 83 (10) (2003) 2049–2051.

[2] R. Rachbauer, S. Massl, E. Stergar, D. Holec, D. Kiener, J. Keckes, J. Patscheider, M. Stiefel, H. Leitner, P.H. Mayrhofer, Decomposition pathways in age hardening of Ti-Al-N films, J. Appl. Phys. 110 (2) (2011) 023515.

[3] A. Hörling, L. Hultman, M. Odén, J. Sjölén, L. Karlsson, Thermal stability of arc evaporated high aluminum-content $Ti_{1-x}Al_xN$ thin films, J. Vac. Sci. Technol. A 20 (5) (2002) 1815–1823.

[4] L. Chavee, E. Serag, M. da Silva Pires, S. Lucas, E. Haye, A mechanistic approach of oxidation resistance, structural and mechanical behaviour of TiAlN coatings, Appl. Surf. Sci. 586 (2022) 152851.

[5] R. Rachbauer, E. Stergar, S. Massl, M. Moser, P.H. Mayrhofer, Three-dimensional atom probe investigations of Ti-Al-N thin films, Scr. Mater. 61 (7) (2009) 725–728.

[6] D. Holzapfel, D. Music, M. Hans, S. Wolff-Goodrich, D. Holec, D. Bogdanovski, M. Arndt, A. Eriksson, K. Yalamanchili, D. Primetzhofer, C. Liebscher, J. Schneider, Enhanced thermal stability of (Ti, Al)N coatings by oxygen incorporation, Acta Mater. 218 (2021) 117204.

[7] P.H. Mayrhofer, D. Music, J.M. Schneider, Ab initio calculated binodal and spinodal of cubic $Ti_{1-x}Al_xN$, Appl. Phys. Lett. 88 (7) (2006) 071922.

[8] B. Alling, A. Karimi, L. Hultman, I.A. Abrikosov, First-principles study of the effect of nitrogen vacancies on the decomposition pattern in cubic $Ti_{1-x}Al_xN_{1-y}$, Appl. Phys. Lett. 92 (7) (2008) 071903.

[9] X. Chu, S.A. Barnett, Model of superlattice yield stress and hardness enhancements, J. Appl. Phys. 77 (9) (1995) 4403–4411.

[10] S. Zhang, D. Sun, Y. Fu, H. Du, Recent advances of superhard nanocomposite coatings: a review, Surf. Coat. Technol. 167 (2–3) (2003) 113–119.

[11] D. Rafaja, C. Wüstefeld, C. Baehtz, V. Klemm, M. Dopita, M. Motylenko, C. Michotte, M. Kathrein, Effect of Internal Interfaces on Hardness and Thermal Stability of Nanocrystalline $Ti_{0.5}Al_{0.5}N$ Coatings, Metall. Mater. Trans. A 42 (3) (2011) 559–569.

[12] K.M. Calamba, J. Salamania, M.P.J. Jõesaar, L.J.S. Johnson, R. Boyd, J.F. Pierson, M.A. Sortica, D. Primetzhofer, M. Odén, Effect of nitrogen vacancies on the growth, dislocation structure, and decomposition of single crystal epitaxial $(Ti_{1-x}Al_x)N_y$ thin films, Acta Mater. 203 (2021) 116509.

[13] N. Norrby, L. Rogström, M.P. Johansson-Jõesaar, N. Schell, M. Odén, In situ X-ray scattering study of the cubic to hexagonal transformation of AlN in $Ti_{1-x}Al_xN$, Acta Mater. 73 (2014) 205–214.

[14] Q. Xia, H. Xia, A.L. Ruoff, Pressure-induced rocksalt phase of aluminum nitride: A metastable structure at ambient condition, J. Appl. Phys. 73 (12) (1993) 8198–8200.

[15] L. Chen, J. Paulitsch, Y. Du, P.H. Mayrhofer, Thermal stability and oxidation resistance of Ti–Al–N coatings, Surf. Coat. Technol. 206 (11) (2012) 2954–2960.

[16] M. Fallmann, Z. Chen, Z.L. Zhang, P.H. Mayrhofer, M. Bartosik, Mechanical properties and epitaxial growth of TiN/AlN superlattices, Surf. Coat. Technol. 375 (2019) 1–7.

[17] Y.J. Kim, T.J. Byun, J.G. Han, Bilayer period dependence of CrN/CrAlN nanoscale multilayer thin films, Superlattices Microstruct. 45 (2) (2009) 73–79.

[18] J.S. Koehler, Attempt to Design a Strong Solid, Phys. Rev. B 2 (2) (1970) 547–551.

[19] M. Kato, T. Mori, L.H. Schwartz, Hardening by spinodal modulated structure, Acta Metall. 28 (3) (1980) 285–290.

[20] P.M. Anderson, C. Li, Hall-Petch relations for multilayered materials, Nanostruct. Mater. 5 (3) (1995) 349–362.

[21] B.M. Clemens, H. Kung, S.A. Barnett, Structure and Strength of Multilayers, MRS Bulletin 24 (2) (1999) 20–26.

[22] A. Knutsson, M.P. Johansson, L. Karlsson, M. Odén, Thermally enhanced mechanical properties of arc evaporated $Ti_{0.34}Al_{0.66}N$/TiN multilayer coatings, J. Appl. Phys. 108 (4) (2010) 044312.

[23] A. Knutsson, M.P. Johansson, L. Karlsson, M. Odén, Machining performance and decomposition of TiAlN/TiN multilayer coated metal cutting inserts, Surf. Coat. Technol. 205 (16) (2011) 4005–4010.

[24] A. Knutsson, M.P. Johansson, P.O.Å. Persson, L. Hultman, M. Odén, Thermal decomposition products in arc evaporated TiAlN/TiN multilayers, Appl. Phys. Lett. 93 (14) (2008) 143110.

[25] A. Knutsson, I.C. Schramm, K. Asp Grönhagen, F. Mücklich, M. Odén, Surface directed spinodal decomposition at TiAlN/TiN interfaces, J. Appl. Phys. 113 (11) (2013) 114305.

[26] R. Bruder, F. Fau-Brenn, R. Brenn, Spinodal decomposition in thin films of a polymer blend, (1079-7114 (Electronic)) (1992).

[27] B.P. Lee, J.F. Douglas, S.C. Glotzer, Filler-induced composition waves in phase-separating polymer blends, Phys. Rev. E 60 (5) (1999) 5812–5822.

[28] K.T. Moore, W.C. Johnson, J.M. Howe, H.I. Aaronson, D.R. Veblen, On the interaction between Ag-depleted zones surrounding γ plates and spinodal decomposition in an Al-22 at.% Ag alloy, Acta Mater. 50 (5) (2002) 943–956.

[29] J. Liu, X. Wu, W. Lennard, D. Landheer, M. Dharma-Wardana, Surface-directed spinodal decomposition in the pseudobinary alloy $(HfO_2)_x(SiO_2)_{1-x}$, J. Appl. Phys. 107 (2010) 123510-123510.

[30] J. Palisaitis, C.L. Hsiao, L. Hultman, J. Birch, P.O. Persson, Direct observation of spinodal decomposition phenomena in InAlN alloys during in-situ STEM heating, Sci. Rep. 7 (2017) 44390.

[31] I. Povstugar, P.-P. Choi, D. Tytko, J.-P. Ahn, D. Raabe, Interface-directed spinodal decomposition in TiAlN/CrN multilayer hard coatings studied by atom probe tomography, Acta Mater. 61 (20) (2013) 7534–7542.

[32] F. Adibi, I. Petrov, L. Hultman, U. Wahlström, T. Shimizu, D. McIntyre, J.E. Greene, J.E. Sundgren, Defect structure and phase transitions in epitaxial metastable cubic $Ti_{0.5}Al_{0.5}N$ alloys grown on MgO(001) by ultra-high-vacuum magnetron sputter deposition, J. Appl. Phys. 69 (9) (1991) 6437–6450.

[33] Y.X. Xu, L. Chen, F. Pei, K.K. Chang, Y. Du, Effect of the modulation ratio on the interface structure of TiAlN/TiN and TiAlN/ZrN multilayers: First-principles and experimental investigations, Acta Mater. 130 (2017) 281–288.

[34] D.B. Lewis, L.A. Donohue, M. Lembke, W.D. Münz, R. Kuzel, V. Valvoda, C.J. Blomfield, The influence of the yttrium content on the structure and properties of $Ti_{1-x-y-z}Al_xCr_yY_zN$ PVD hard coatings, Surf. Coat. Technol. 114 (2) (1999) 187–199.

[35] W.C. Oliver, G.M. Pharr, An improved technique for determining hardness and elastic modulus using load and displacement sensing indentation experiments, J. Mater. Res. 7 (6) (1992) 1564–1583.

[36] Z. Liu, L. Chen, Y. Xu, Structure, mechanical and thermal properties of $Ti_{1-x}Al_xN$/CrAlN (x = 0.48, 0.58 and 0.66) multilayered coatings, J. Am. Ceram. Soc. 101 (2018) 845–855.

[37] G. Kresse, J. Furthmüller, Efficient iterative schemes for ab initio total-energy calculations using a plane-wave basis set, Phys. Rev. B 54 (16) (1996) 11169–11186.

[38] J.P. Perdew, K. Burke, M. Ernzerhof, Generalized Gradient Approximation Made Simple, Phys. Rev. Lett. 77 (18) (1996) 3865–3868.

[39] G. Kresse, D. Joubert, From ultrasoft pseudopotentials to the projector augmented-wave method, Phys. Rev. B 59 (3) (1999) 1758–1775.

[40] P.E. Blöchl, Projector augmented-wave method, Phys. Rev. B 50 (24) (1994) 17953–17979.

[41] H.J. Monkhorst, J.D. Pack, Special points for Brillouin-zone integrations, Phys. Rev. B 13 (12) (1976) 5188–5192.

[42] K. Grönhagen, J. Ågren, M. Odén, Phase-field modelling of spinodal decomposition in TiAlN including the effect of metal vacancies, Scr. Mater. 95 (2015) 42–45.

[43] P.H. Mayrhofer, F.D. Fischer, H.J. Böhm, C. Mitterer, J.M. Schneider, Energetic balance and kinetics for the decomposition of supersaturated $Ti_{1-x}Al_xN$, Acta Mater. 55 (4) (2007) 1441–1446.

[44] J. Zhang, C. Hu, L. Chen, Y. Kong, Y. Du, P.H. Mayrhofer, Impact of oxygen content on the thermal stability of Ti-Al-O-N coatings based on computational and experimental studies, Acta Mater. 227 (2022) 117706.

[45] B. Uberuaga, H. Jonsson, A Climbing Image Nudged Elastic Band Method for Finding Saddle Points and Minimum Energy Paths, J. Chem. Phys. 113 (2000) 9901–9904.

[46] M.C. Marinica, L. Ventelon, M.R. Gilbert, L. Proville, S.L. Dudarev, J. Marian, G. Bencteux, F. Willaime, Interatomic potentials for modelling radiation defects and dislocations in tungsten, J. Phys. Condens. Matter 25 (39) (2013) 395502.

[47] R. Rachbauer, J.J. Gengler, A.A. Voevodin, K. Resch, P.H. Mayrhofer, Temperature driven evolution of thermal, electrical, and optical properties of Ti–Al–N coatings, Acta Mater. 60 (5) (2012) 2091–2096.

[48] J. Verhoeven, Fundamentals of Physical Metallurgy, 1975.

[49] F. Adibi, I. Petrov, L. Hultman, U. Wahlstrom, T. Shimizu, D. McIntyre, J. Greene, J.E. Sundgren, Defect structure and phase transitions in epitaxial metastable cubic $Ti_{0.5}Al_{0.5}N$ alloys grown on MgO(001) by ultra-high-vacuum magnetron sputter deposition, J. Appl. Phys. 69 (1991) 6437–6450.

[50] M. Tkadletz, C. Hofer, C. Wüstefeld, N. Schalk, M. Motylenko, D. Rafaja, H. Holzschuh, W. Bürgin, B. Sartory, C. Mitterer, C. Czettl, Thermal stability of nanolamellar fcc-$Ti_{1-x}Al_xN$ grown by chemical vapor deposition, Acta Mater. 174 (2019) 195–205.

[51] D. Holec, R. Rachbauer, L. Chen, L. Wang, D. Luef, P.H. Mayrhofer, Phase stability and alloy-related trends in Ti–Al–N, Zr–Al–N and Hf–Al–N systems from first principles, Surf. Coat. Technol. 206 (7) (2011) 1698–1704.

[52] U. Ratayski, M. Motylenko, A. Ershova, M. Šíma, M. Jílek, D. Rafaja, Competition between local lattice strains and distribution of metallic species in $Ti_{1-x}Al_xN$ coatings with fluctuating [Ti]/[Al] ratio, Surf. Coat. Technol. 344 (2018) 322–329.

[53] P.H. Mayrhofer, L. Hultman, J.M. Schneider, P. Staron, H. Clemens, Spinodal decomposition of cubic $Ti_{1-x}Al_xN$: Comparison between experiments and modeling, Int. J. Mater. Res. 98 (11) (2007) 1054–1059.

[54] P.H. Mayrhofer, L. Hultman, J.M. Schneider, P. Staron, H. Clemens, Spinodal decomposition of cubic $Ti_{1-x}Al_xN$: Comparison between experiments and modeling, Int. J. Mater. Res. 98 (11) (2007) 1054–1059.

[55] P. Mayrhofer, A. Hörling, L. Karlsson, J. Sjoelen, T. Larsson, C. Mitterer, L. Hultman, Self-Organized Nanostructures in the Ti–Al–N System, Appl. Phys. Lett. 83 (2003) 2049–2051.

[56] P.H. Mayrhofer, D. Music, J.M. Schneider, Influence of the Al distribution on the structure, elastic properties, and phase stability of supersaturated $Ti_{1-x}Al_xN$, J. Appl. Phys. 100 (9) (2006) 094906.

[57] D. Rafaja, C. Wüstefeld, M. Motylenko, C. Schimpf, T. Barsukova, M.R. Schwarz, E. Kroke, Interface phenomena in (super)hard nitride nanocomposites: from coatings to bulk materials, Chem. Soc. Rev. 41 (15) (2012) 5081–5101.

[58] X. Tian, J.-N. Wang, Y.-P. Wang, X.-F. Shi, B.-Y. Tang, First-principles investigation of point defect and atomic diffusion in $Al2Ca$, J. Mech. Phys. Solids 103 (2017) 6–12.

[59] M. Bartosik, C. Rumeau, R. Hahn, Z.L. Zhang, P.H. Mayrhofer, Fracture toughness and structural evolution in the TiAlN system upon annealing, Sci. Rep. 7 (1) (2017) 16476.

[60] W. Lengauer, Properties of bulk δ-TiN_{1-x} prepared by nitrogen diffusion into titanium metal, J. Alloys. Compd. 186 (2) (1992) 293–307.